DRAFT VERSION FEBRUARY 5, 2008
Preprint typeset using LaTeX style emulateapj v. 11/26/04

THE LENSED ARC PRODUCTION EFFICIENCY OF GALAXY CLUSTERS: A COMPARISON OF MATCHED OBSERVED AND SIMULATED SAMPLES

ASSAF HORESH[1], ERAN O. OFEK[1], DAN MAOZ[1], MATTHIAS BARTELMANN[2], MASSIMO MENEGHETTI[2], HANS-WALTER RIX[3]

Draft version February 5, 2008

ABSTRACT

We compare the statistical properties of giant gravitationally lensed arcs produced in matched simulated and observed cluster samples. The observed sample consists of 10 X-ray selected clusters at redshifts $z_c \sim 0.2$ imaged with HST by Smith et al.. The simulated dataset is produced by lensing the Hubble Deep Field, which serves as a background source image, with 150 realizations (different projections and shifts) of five simulated $z_c = 0.2$ clusters from a ΛCDM N-body simulation. The real and simulated clusters have similar masses, the real photometric redshift is used for each background source, and all the observational effects influencing arc detection in the real dataset, including light from cluster galaxies, are simulated in the artificial dataset. We develop, and apply to both datasets, an objective automatic arc-finding algorithm. We find consistent arc statistics in the real and in the simulated sample, with an average of ~ 1 detected giant (length to width ratio $l/w \geq 10$) arc per cluster and ~ 0.2 giant luminous ($R_{ST} < 22.3$ mag) arc per cluster. Thus, taking into account a realistic source population and observational effects, the clusters predicted by ΛCDM have the same arc-production efficiency as the observed clusters. If, as suggested by other studies, there is a discrepancy between the predicted and the observed total number of arcs on the sky, it must be the result of differences between the redshift dependent cluster mass functions, and not due to differences in the lensing efficiency of the most massive clusters.

Subject headings: Cosmology: Dark Matter, Galaxies: Clusters: General, Cosmology: Gravitational Lensing, Methods: Data Analysis

1. INTRODUCTION

The statistical properties of giant gravitationally lensed arcs in galaxy clusters are sensitive to clusters properties, such as mass function, mass profile, and concentration, which in turn depend on cosmology. Cosmological models can therefore be tested, in principle, by comparing the predicted numbers and properties of giant arcs with observations.

Bartelmann et al. (1998; hereafter B98) compared the observed number of giant arcs with predictions based on calculations of ray tracing through galaxy clusters formed in N-body simulations, for various cosmological models. Artificial sources were all placed at redshift $z_s = 1$, which is close to the average redshift of observed arcs (Kneib & Soucail 1996). B98 argued that using a single source redshift is acceptable because the change in the critical surface mass density is $\leq 20\%$, for clusters at redshift $z_c \sim 0.3$, when the source redshift varies in the range $0.7 \leq z_s \leq 2$. From the simulated lensed images, B98 obtained the theoretical optical depth for forming arcs with length-to-width ratios $l/w > 10$. By multiplying the lensing optical depth by the density of background sources with magnitudes $R < 23.5$ mag, as measured by Smail et al. (1995), they predicted the average number of arcs per cluster with the above l/w ratio and $R < 21.5$ mag. The predicted numbers of arcs were compared with the numbers observed in a sample of 16 X-ray-selected clusters from the Einstein Observatory Extended Medium Sensitivity Survey (EMSS; Le Fevre et al. 1994). B98 found that the observed number of arcs was higher by an order of magnitude than the predictions of the (now-standard) Λ-dominated cold dark matter (ΛCDM) cosmological model.

This initial study of arc statistics by B98 motivated several subsequent studies, both theoretical and observational. From the observational side, improvements in the volume and quality of data have made the statistics more accurate. Zaritsky and Gonzalez (2003) measured the frequency of arc occurrence in a sample of clusters with redshifts $0.5 < z_c < 0.7$, observed as part of the Las Campanas Distant Cluster Survey (LCDCS). They compared their results for arcs having $l/w > 10$ and $R < 21.5$ mag with a larger observed sample of 38 clusters from the EMSS (Luppino et al. 1999). After correcting the observed incidence of arcs in the EMSS sample for incompleteness, they found that the arc incidence is lower than, but consistent with, the arc incidence in the LCDCS sample. Arc statistics were also derived for the Red-Sequence Cluster Survey (RCS) by Gladders et al. (2003) who found the number of arcs to be larger by a factor of $10-20$ than the theoretical value predicted by B98 for clusters in the redshift range $0 < z_c < 1$. Thus all three of these more recent observed samples support the conclusion of B98, of an observed incidence of giant arcs that is large compared to the B98 ΛCDM predictions.

In parallel, several theoretical studies have also readdressed the problem. Wambsganss et al. (2004) studied the dependence of the cross section for arc formation on the lensed source redshift. They performed several lensing simulations, each with artificial sources on a single redshift plane, as in B98. However, instead of using single simulated clusters, they lensed their sources through the whole volume of an N-body simulation. Furthermore, the magnification of the arcs was used as a proxy for the l/w ratios, instead of a direct measurement. They found that the cross section is a steep function of source redshift, and concluded that the order of magnitude problem reported by B98 can be resolved by adding sources

[1] School of Physics and Astronomy and Wise Observatory, Tel Aviv University, Tel Aviv 69978, Israel.
[2] ITA, Universität Heidelberg, Albert-Ueberle Str. 2, D–69120 Heidelberg, Germany.
[3] Max Planck Institute für Astronomie, Koenigstuhl 17, D-69117 Heidelberg, Germany.

at redshifts other than $z_s = 1$ to the simulations. However, Li et al. (2005) have found that approximating the l/w ratio by the magnification is incorrect, and that the cross section dependence on source redshift is shallower than the one found by Wambsganss et al.

Dalal et al. (2004) repeated the B98 ray tracing analysis of artificial sources using a larger sample of simulated clusters (of which B98 had used a subset) and compared their results to the 38-cluster EMSS sample (Luppino et al. 1999), but concluded that the arc statistics data and the ΛCDM model are consistent. They explained the order of magnitude discrepancy reported by B98 as a combination of several smaller effects : 1) The sky density of EMSS clusters is lower by a factor of 2 than was assumed by B98; 2) the background source density used by Dalal et al. in their calculations (based on Fontana et al. 2000) is higher by a factor of 2 than the one used by B98; 3) the placement of sources at additional redshifts, other than $z_s = 1$, yields a higher optical depth than the one derived in B98.

The artificial clusters used by the above studies represent the cluster dark matter component only. Adding a mass component, associated with the dark and baryonic mass of the cluster galaxies, to the artificial clusters can affect the cross section for forming giant arcs in several ways (Meneghetti et al. 2000). The critical lines will curve around the cluster galaxies, thus increasing the cross section. On the other hand, the galaxies will split some of the long arcs into shorter arclets, thus decreasing the giant arc cross section. After studying these two competing effects, Meneghetti et al. (2000) concluded that the effect of cluster galaxies on the lensing cross section is negligible, a conclusion also supported by an analytical study by Flores et al. (2000). More recently, Meneghetti et al. (2003) found that the cD galaxy in each cluster does increase the cross section, but only by up to $\sim 50\%$ for realistic parameters. Puchwein et al. (2005) have studied the influence of the intracluster gas on lensing cross section.

Torri et al. (2004) studied the effect of cluster mergers on arc statistics by following the lensing cross-section of a simulated cluster with small time steps as the cluster evolves. They concluded that, during a merger, the strong-lensing cross section can be enhanced by an order of magnitude in an optimal projection, potentially providing yet another contribution towards resolving the problem reported by B98. The effects on arc statistics of dark-energy with an equation of state different from that of a cosmological constant have also been studied. (Bartelmann et al. 2003a; Meneghetti et al. 2004a)

In view of the conflicting observational and theoretical results, in this paper we revisit arc statistics using several novel approaches. A discrepancy between models and observations could arise in a number of ways, such as a larger cluster number density in reality compared to the results of simulations, a different mass function, or real clusters that are more efficient lenses than simulated ones. To isolate the problem (or problems) that have led to the controversy, we examine here only the arc production efficiency of mass-matched real and simulated clusters at one particular redshift, $z_c = 0.2$. Once this issue is addressed, the other factors, such as cluster number density, mass function, and redshift evolution, can be studied separately. To circumvent the question of source properties (density, redshift, surface brightness), our lensing simulations are based on real background sources and their photometric redshifts, instead of artificial sources at a single redshift. For this purpose, we use the sources in the Hubble Deep Field (HDF; Williams et al. 1996), with photometric redshifts from the catalog by Fernández-Soto et al. (1999). To the artificial lensed data, produced by the simulations, we add observational effects, such as Poisson noise and artificial cluster galaxies, which we match to the specific observed cluster sample to which the simulations are compared. We then use an objective automated algorithm to detect arcs in both the simulated data and in the real data. Our inclusion of observational effects in the simulations allows us to compare directly the incidence of arcs in the simulations and in the observations, without the need to impose magnitude cuts on the arcs.

Throughout this paper we adopt a ΛCDM cosmology with parameters $\Omega_m = 0.3$, $\Omega_\Lambda = 0.7$, and $H_0 = 70\ h_{70}$ km s^{-1}Mpc^{-1}. The paper's outline is as follows. The observed sample we analyze is described in §2. §3 provides a detailed description of the lensing simulations. A short description of the arc-finding algorithm is given in §4. §5 presents the results, and in §6 we summarize the conclusions.

2. OBSERVED CLUSTER SAMPLE

To obtain a reliable observational estimate of arc statistics, we have analyzed a well-defined sample of 10 massive clusters observed with the Hubble Space Telescope (HST) by Smith et al. (2004). The choice of massive clusters and of deep observations at HST resolution are intended to maximize the number of detected arcs, and thus reduce the statistical error.

The sample of Smith et al. (2004) consists of 10 galaxy clusters from the X-ray Brightest Abell-type Clusters of galaxies (XBACs) catalog (Ebeling et al. 1996), with $0.171 < z_c < 0.255$, and Galactic $E(B-V) \leq 0.1$. The X-ray $(0.1-2.4$ keV) flux limit of $f_X \geq 5.0 \times 10^{-12}$ erg cm^{-2} s^{-1} applied to this redshift range implies X-ray luminosities $L_X \geq 4.1 \times 10^{44} h_{70}^{-2}$ erg s^{-1}. Assuming the Reiprich & Böhringer (2002) $L_X - M_{200}$ relation, where M_{200} is the mass enclosed within r_{200}, (the radius within which the average density is equal to 200 times the critical cosmological density), the observed cluster masses are in the range $1.7 \times 10^{14} \lesssim M_{200} \lesssim 2.6 \times 10^{16}\ h_{70}^{-1} M_\odot$, with a mean of $M_{200} = 1.6 \times 10^{15}\ h_{70}^{-1} M_\odot$, and a mean r_{200} of $2.2 h_{70}^{-1}$ Mpc. This range of masses takes into account the uncertainties in the best fit to the $L_X - M_{200}$ relation of Reiprich & Böhringer (2002), i.e., the range is increased by the sum of of the uncertainties in M_{200} for the lowest and highest luminosities. The cluster properties, along with their projected $M(r \leq 390\ h_{70}^{-1}$kpc), as estimated by Smith et al. (2004) based on an analysis of weak and strong lensing, are summarized in Table 1.

The Smith et al. (2004) sample was observed with WFPC2 on HST using the F702W filter, with total exposure times of $6500-7800$s. The individual exposures of each cluster, centered on one of the three WF CCDs, were combined, dithered, and cosmic-ray rejected using an IRAF based script (Gal-Yam, Maoz & Sharon 2002; Sharon 2003). Each WF CCD is then a 1600×1600 pixel image, $1\farcm3$ on a side, with a pixel scale of $0\farcs05$. Rows and columns near the image borders, where spurious features due to the WFPC2 optics may appear, were excluded from the image.

3. LENSING SIMULATIONS

3.1. *Simulated Cluster Sample*

We performed our lensing simulations using the same primary sample of five artificial clusters used by B98. As described in detail in B98, these clusters are the most massive clusters found in a cosmological ΛCDM ($\Omega_m = 0.3, \Omega_\Lambda =$

TABLE 1
OBSERVED CLUSTER SAMPLE

Cluster	z	$L_X(0.1-2.4\,\mathrm{keV})$ $[10^{44}h_{70}^{-2}\mathrm{erg\,s^{-1}}]$	$M(r\le 390h_{70}^{-1}\mathrm{kpc})$ $[10^{14}h_{70}^{-1}M_\odot]$	M_{200} $[10^{15}h_{70}^{-1}M_\odot]$
Abell 68	0.255	5.32	3.51	1.20
Abell 209	0.209	8.44	1.25	1.60
Abell 267	0.230	8.32	2.06	1.59
Abell 383	0.187	4.86	2.80	1.12
Abell 773	0.217	7.75	4.01	1.52
Abell 963	0.206	6.28	2.58	1.32
Abell 1763	0.228	8.88	1.66	1.66
Abell 1835	0.253	24.68	4.62	3.19
Abell 2218	0.171	4.78	4.33	1.10
Abell 2219	0.228	12.36	2.69	2.04

Note - Luminosities are taken from the XBACs catalog (Ebeling et al. 1996). $M(r\le 390h_{70}^{-1}\mathrm{kpc})$ is from Smith et al. (2004) based on weak and strong lensing. M_{200} is based on the $L_X - M_{200}$ relation of Reiprich & Böhringer (2002). All numbers have been converted to the adopted ΛCDM cosmology.

TABLE 2
SIMULATED $z = 0.2$ CLUSTER SAMPLE

Cluster Id	M_{200} $[10^{15}\,h_{70}^{-1}M_\odot]$	κ_{max} x-projection	y-projection	z-projection
cj1109	1.35	0.615	0.650	0.562
cj1209	1.58	0.890	0.942	0.677
cj1309	1.03	0.814	0.680	1.224
cj1409	0.93	1.234	0.605	1.168
cj1509	0.77	0.330	0.806	0.393

Note - κ_{max} is the maximum convergence assuming all sources are at $z_s = 1$.

$0.7, h_{70} = 1$) N-body simulation, as a part of the "GIF" project (Kauffmann et al. 1999). The GIF simulations adopted the CDM power spectrum by Bond and Efstathiou (1984) with a shape parameter of $\Gamma = 0.21$, and a normalization of $\sigma_8 = 0.90$ (Eke et el. 1996). The simulations were run with N=256^3 particles of $2\times10^{10}\,h_{70}^{-1}\mathrm{M}_\odot$ each, in a comoving volume of $201^3\,(\mathrm{Mpc}/h_{70})^3$.

The clusters were defined by first locating their cores at $z_c = 0.2$ using a "friends-of-friends" group finder. All the particles within an Abell radius, $r_A = 2.14h_{70}^{-1}$ Mpc, around each core were collected to form a cluster. The masses of the five clusters within r_{200} (which has a mean of $2\,h_{70}^{-1}$Mpc) are in the range $0.8-1.6\times10^{15}\,h_{70}^{-1}\mathrm{M}_\odot$. The three-dimensional mass distribution of each of these clusters was projected onto each of the three faces of the simulation volume, thus obtaining three two-dimensional surface mass density fields. The gravitational deflection angle field of each projection was calculated on a grid with an angular resolution of $0.''88$ (see Bartelmann & Weiss 1994, for details). An area of $160''\times160''$, corresponding to $0.52\times0.52\,h_{70}^{-2}\mathrm{Mpc}^2$ in our adopted cosmology, and surrounding the center of each simulated cluster, was cut out of the larger grid. In order to match the resolution of our background source image (the HDF, see §3.2 below) we linearly interpolated the deflection-angle grid onto a finer grid with an angular resolution of $0.''04$. The five clusters, with three projections each, comprise our artificial cluster sample. Table 2 summarizes the properties of the simulated clusters and their projections. For each projection, we list κ_{max}, the maximum of the convergence, defined as $\kappa = \Sigma/\Sigma_{\mathrm{cr}}$, where Σ is the projected surface mass density, $\Sigma_{\mathrm{cr}} = D_l D_{ls}/4\pi G D_s$, and D_l, D_s, and D_{ls} are the angular diameter distances between the observer and the lens, the observer and the source, and the lens and the source, respectively.

The masses of the simulated clusters are well matched to those of the observed clusters. Although there is some uncertainty in the estimates of the observed cluster masses, we do not expect the difference between the mean masses of the two samples to differ by more than a factor of ~ 2.

3.2. *Background source image*

For a background of sources to be lensed by our artificial clusters, with properties representative of the galaxies lensed by real clusters, we use the F606W and F814W images of the HDF. The observed sample, to which we will compare our simulations, was imaged with the HST WFPC2 F702W filter, centered at 7020 Å. In order to match the simulations and the observations, we approximate the F702W filter as the average of the F606W and F814W filters. The summed F606W and F814W exposures of the HDF reach $I_{\mathrm{AB}} = 29.8$ with $\mathrm{S/N} = 5$ (Williams et al. 1996), which is deeper by ~ 4 mag than the observed Smith et al. (2004) cluster images to which we compare our models. Since the lensed arcs typically have magnifications of order 10, the HDF suitably represents the sources to be lensed into such arcs. The $\sim 5\,\mathrm{arcmin}^2$ area of the HDF is too small to serve as a source background for $z_c = 0.2$ clusters. We therefore used segments of the HDF as building blocks with which we created a larger, $192''\times192''$, source image with a scale of $0.''04\,\mathrm{pixel}^{-1}$. Three segments of 1600×1600 pixels ($64''\times64''$) were cut out of the HDF image around the centers of each of the three WF CCD's. A mosaic was then built out of 3×3 blocks, each block randomly selected from the three building blocks.

Our lensing calculation requires redshift information for each background source. We therefore created a redshift image, in which the pixels of each source are assigned the value of the source photometric redshift. The redshift image was created as follows. First, we detected objects in the HDF mosaic using SExtractor (Bertin and Arnouts 1996), an object detection and photometry program. SExtractor produces an object catalog and a "segmentation image", an image of the detected objects in which pixels belonging to each object are assigned the object's catalog number. The values of the pixels comprising each object in the segmentation image were then replaced with the object's redshift by cross referencing the detected object catalog with the HDF photometric redshift catalog of Fernández-Soto et al. (1999). All but 39 of the 985 objects we detect in the HDF with $I_{AB} \le 28$ mag appear in the Fernández-Soto et al. (1999) catalog. In addition we detect 393 objects with $28 < I_{AB} \le 29.8$ mag, beyond the flux limit of the catalog. The 39 non-catalog objects with $I_{AB} \le 28$ were assigned redshifts based on their magnitudes, by drawing values from the observed distribution of redshifts for objects in the catalog with the appropriate magnitude. For the 393 $I_{AB} > 28$ mag objects, the redshift distribution for the $I_{AB} = 28$ bin was used, which is reasonable given the small change in redshift distribution beyond $I_{AB} \approx 26$ (Fernández-Soto et al. 1999).

3.3. *Ray tracing method*

In the small-angle, weak-field, and thin lens regime (e.g., Bartelmann 2003b) lensing is described by the lens equation,

$$\vec{\beta} = \vec{\theta} - \frac{D_{ls}}{D_s}\vec{\alpha}(\vec{\theta}), \quad (1)$$

where $\vec{\beta}$ is a two-dimensional vector describing the angular position of the source on the sky, $\vec{\theta}$ is the angular position of a lensed image, and $\vec{\alpha}(\vec{\theta})$ is the deflection angle due to the gravitational potential of the cluster.

In previous arc statistics studies, artificial sources on a source plane at a single redshift were lensed through a lens plane (e.g., Bartelmann et al. 1998; Meneghetti et al. 2003; Dalal et al. 2004). Starting from the observer, rays were shot back to every position $\vec{\theta}$ in the lens plane. Each ray was then deflected towards a position $\vec{\beta}$ according to the lens equation. Only if an artificial source existed at $\vec{\beta}$, would the source be mapped onto the lens plane. Thus, a "lensed image" of the source plane in the lens plane was produced.

In the present work, as opposed to using artificial sources at a single redshift, we use real background sources, each at its photometric redshift. Since D_{ls}/D_s is no longer constant for a given lens redshift, a single value for the position $\vec{\beta}$ cannot be obtained, given particular values of $\vec{\theta}$ and $\vec{\alpha}(\vec{\theta})$. Instead, the lens equation, which depends linearly on D_{ls}/D_s, produces a range of values for $\vec{\beta}$. To account for this, we calculate the maximum and minimum values of D_{ls}/D_s for the redshift range spanned by the sources in the redshift catalog (note that D_{ls}/D_s is not necessarily a monotonic function of z_s). By introducing these values into the lens equation, we obtain $\vec{\beta}_1$ and $\vec{\beta}_2$, respectively. The vector $\vec{\beta}_2 - \vec{\beta}_1$ define a line on the source plane tracing the different positions $\vec{\beta}(z_s)$ corresponding to different source redshifts. We then scan the line for pixels belonging to detected sources. When such a pixel, belonging to a certain source at z_s, is found, we calculate the $\vec{\beta}$ corresponding to z_s. If the observed and the calculated $\vec{\beta}$'s match, we lens the source pixel by adding its count rate to the pixel at position $\vec{\theta}$ in the lens image. The count rate in every pixel in the simulated lensed HDF image is multiplied by the mean exposure time of each of the observed clusters, 7430 s.

Ten lensing realizations were performed for every cluster projection, where in each realization the source image was randomly shifted in relation to the center of the lens. The five simulated clusters, times three projections, times 10 positions relative to the background, thus produce a sample of 150 simulated F702W lensed images.

3.4. *Observational effects*

The next step in our study, which again extends upon previous work, is to apply to the simulations all of the observational effects that exist in the real data to which we will compare these simulations (see Meneghetti et al. 2004b, for a first attempt at applying observational effects to such simulations). These observational effects include light from the foreground cluster galaxies, sky and detector backgrounds, Poisson noise, and readout noise.

The light of simulated cluster galaxies was added based on the luminosity function of early type galaxies in clusters derived by Goto et al. (2002). They identified clusters with $0.02 < z_c < 0.25$ based on colors and galaxy over-density in the Sloan Digital Sky Survey (SDSS), and calculated the Schechter (1976) luminosity function parameters M^* and α in the SDSS u, g, r, i, and z bands for early- and late-type galaxies. Goto et al. (2002) used three different criteria for distinguishing between the early-type and the late-type galaxies, resulting in three different luminosity functions. We used the parameters $M^*_{\rm AB} = -22.1$ mag and $\alpha = -0.75$ which are the averages of the parameters obtained in the r, and i bands for early-type galaxies identified as such based on their light concentration.

We determined the number of galaxies to be added to our simulated cluster images using the properties of our observed cluster sample. We first normalized the luminosity function so as to have 21.5 galaxies in the absolute AB magnitude range $-22.7 \leq M_{\rm F702} \leq -20.7$, matching the average number of galaxies per cluster in this absolute magnitude range that we find in the observed sample. The normalized luminosity function then has 67 galaxies in the range $-23.2 \leq M_{\rm F702} \leq -16.7$. We then added to each simulated cluster image 67 galaxies, with absolute magnitudes drawn from the luminosity function.

The artificial cluster galaxies were placed in each simulated cluster image at a position drawn at random from a distribution following the surface mass density of the cluster. In addition, we placed an artificial cD galaxy at the position of the surface mass density peak, with a random AB magnitude in the range $-24 \leq M_{\rm F702} \leq -23.2$, also based on the range seen in the observed sample. The light of each galaxy was distributed with a Sérsic projected radial profile,

$$\log\left(\frac{I}{I_0}\right) = -b_n\left[(R/R_e)^{\frac{1}{n}} - 1\right], \quad (2)$$

where I is the surface brightness, R_e is the half-light radius, and $I_0 = I(R_e)$, with a random axis ratio in the range $[0.5, 1]$, and with a random orientation. R_e for each galaxy was calculated using the relation between luminosity and half-light radius $L_i \propto R_e^{1.59}$ obtained from Fig. 5 of Bernardi et al. (2003), while the other Sérsic profile parameters were taken to be

$$\log n = 0.28 + 0.52\log R_e,$$
$$b_n = 0.868n - 0.142, \quad (3)$$

following Caon, Capaccioli, and D'Onofrio (1993), with R_e in kpc. The surface brightnesses of these simulated $z = 0.2$ galaxies were converted to counts pixel^{-1}, using the WFPC2 F702W sensitivity (Baggett et al. 2002) and the mean exposure time of the observed sample.

A uniform background was added to all the simulated lensed images, based on the average background value of $186\,e^-$ pixel^{-1} in the observed cluster sample, scaled to the pixel size of the simulated sample. Poisson noise was then added to each pixel in the image according to the total counts (contributed by background, cluster galaxies, and lensed background objects). Finally, readout noise of $1.4\,e^-$ was added to each pixel, corresponding to the readout noise per original pixel of $5.2\,e^-$, times $\sqrt{3}$ (each cluster exposure was split into 3 sub-exposures) and divided by the 6.25 dithered sub-pixels comprising a real pixel.

Two of the observed clusters (Abell 2218, and Abell 2219) have a background level which is lower by $\sim 40\%$ than that of the other clusters. In order to study the effect of adding low background to our images, we produced a secondary sample of 90 lensed data sets with a low background level of $71\,e^-$ per pixel. The implications of using a lower background are discussed in §5.1.

Fig. 1 shows several examples of the simulations, before and after the addition of observational effects.

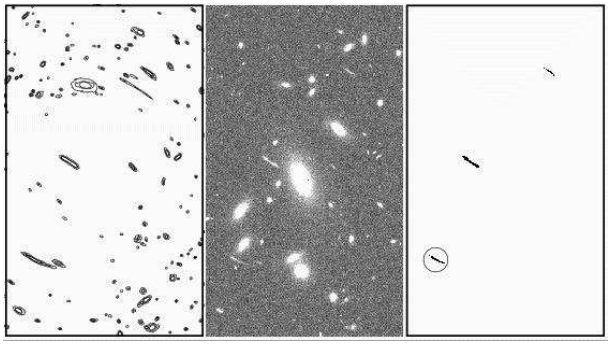

(a) cluster cj1209

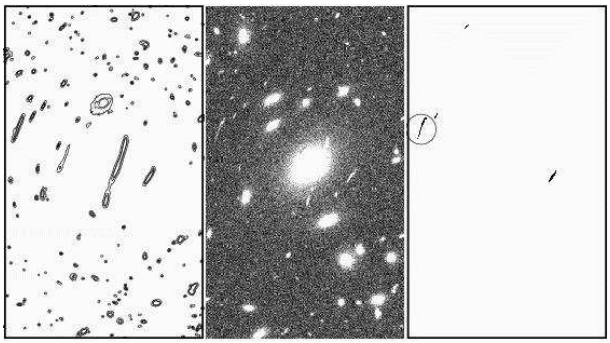

(b) cluster cj1309

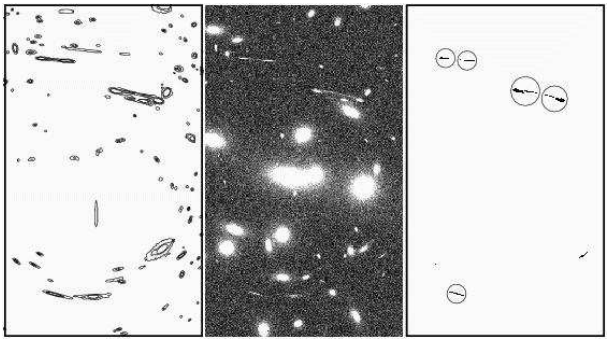

(c) cluster cj1409

FIG. 1.— Examples of simulated lensed images. The left panels show a contour map of the lensed image produced by the lensing simulations. The middle panels show the lensed images after the observational effects are added. The right panels show the arcs detected by our arc-finding algorithm with $l/w \geq 7$. Giant arcs $(l/w \geq 10)$ are circled.

4. ARC DETECTION ALGORITHM

In order to objectively compare the arc statistics of simulated and observed clusters, we have devised an automatic arc finding program that can be applied to both real and simulated data. Our algorithm[4] is implemented in a simple script that makes repeated calls to the SExtractor (Bertin & Arnouts 1996) object finding program (full details are given in Appendix A). Briefly, in each SExtractor call, objects are detected using slightly different detection parameters. Objects with an axis ratio below some threshold are then removed from the segmentation images produced in the different calls. Finally, arcs are detected in an image produced by combining the above segmentation images. The arc length-to-width ratio, following Miralda-Escude (1993), is measured as follows. First, we find the center of the arc, defined as the pixel with the maximum flux. Then, the point in the arc farthest from the center is located, and finally the farthest point from the second point is located. The arc length is defined as the sum of the distances from the arc center to the two extreme points, and the width of the arc is defined as its area divided by its length. The performance of the algorithm on several of the simulated clusters is illustrated in Fig. 1. In Appendix A, we also compare our arc-finding algorithm to a similar tool presented by Lenzen et al. (2004).

[4] available at http://wise-obs.tau.ac.il/∼assafh

5. ARC STATISTICS

5.1. *Results for the simulated sample*

Applying our arc finder to the 150 simulated lensed images, we detect a total of 141 giant $(l/w \geq 10)$ arcs. The average number of arcs per cluster is $\bar{N} = 0.94^{+0.08}_{-0.08}$. Almost all of the arcs, 136 out of 141, were produced by three out of the five simulated clusters. Fig. 2 shows the number of arcs detected in the different background source realizations for each of the cluster projections. Apart of the inefficiency of arc production by two of the clusters, we see that the efficiency of the other clusters sometimes depends strongly on projection axis (see also Dalal et al. 2004). Not surprisingly, comparison of Figure 2 and Table 2, shows that the most efficient cluster projections tend to have high values of κ_{max}, and vice-versa.

In the previous studies by B98 and Dalal et al. (2004), observational effects were not included in the simulations, and therefore observations and simulations were compared only for arcs that are luminous in addition to being giant. Wu & Hammer (1993) defined giant luminous arcs as having $l/w > 10$ and $B < 22.5$ mag (or $R < 21.5$ mag; B98). If we adopt an analogous definition of $m_{\rm F702} \leq 21.8$ mag for luminous arcs, the total number of giant luminous arcs we detect is 33, or $\bar{N} = 0.22^{+0.05}_{-0.04}$ arcs per cluster.

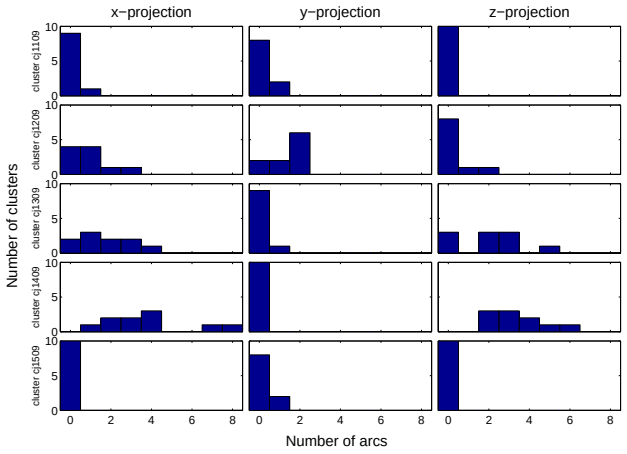

FIG. 2.— Distribution of the number of detected arcs per cluster with $l/w > 10$ in the simulated sample. Each row represent a different cluster and each column represent a different projection. The first and last clusters are inefficient arc producers, and one of the projections of the third and fourth clusters is also inefficient.

To investigate the effect of using a realistic source redshift distribution, we have repeated our simulations with all sources at redshift $z_s = 1$, as in B98. The total number of arcs and giant luminous arcs in our standard simulations, 141 and 33, changes by only -16 and $+11$, respectively, consistent to within 2σ with Poisson fluctuations. The consistency is also evident when comparing the number distribution of arcs per cluster in the two sets of simulations, as shown in Fig. 3. In

the Fernández-Soto et al. (1999) catalog, the number of bright objects per arc-minute peaks near $z = 1$, and the median redshift of bright objects is also 1.0. In order to investigate the possibility that the HDF has an atypical redshift distribution due to cosmic variance, we have repeated the simulations, but with all sources at $z_s = 1.5$. We detect a total of 168 arcs and 50 giant luminous arcs, which is an increase of 19% and 51%, respectively, compared to the number of arcs we detect in our standard simulations. These results are also shown in Fig 3. Thus, there will be a small or modest increase in the predicted number of arcs if in the HDF the characteristic redshifts are anomalously low. Similarly, an atypically low space density of sources in the HDF (e.g. Dickinson 2000), would underpredict the number of arcs.

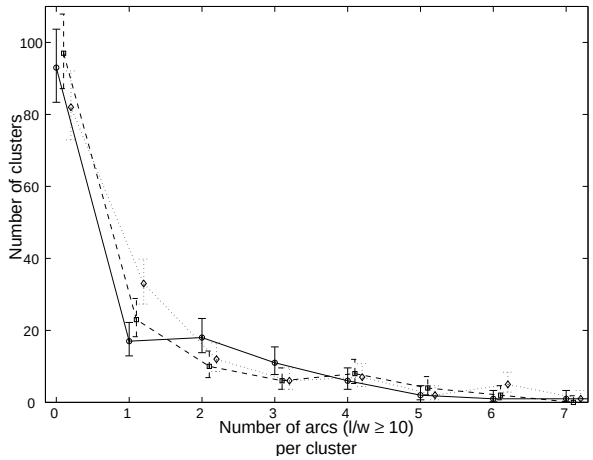

FIG. 3.— Distribution of detected arcs per cluster with $l/w \geq 10$ in the simulations, for different assumed source redshifts. Circles and solid lines represent the simulations in which sources with real photometric redshifts were lensed. Squares and dashed lines result when all sources are assigned a redshift $z_s = 1$. Diamonds and dotted lines are for all sources at $z_s = 1.5$. Poisson error bars are shown. Here and in subsequent figures, a slight offset in the horizontal direction has been induced between the curves, for the sake of clarity

The observational effects included in our simulations influence the detection process in several ways. Image depth and the local background determine whether a lensed source will be detected. Furthermore, since the lensed sources have real light profiles rather than a constant surface brightness, it is possible that only certain parts of the lensed source are detected. As a result, the l/w ratio of an arc with a real light profile, as detected in an image to which observational effects have been added, will sometimes differ from the l/w of the same arc in a noise-free image produced by lensing a source with a constant surface brightness profile. In addition, the cluster galaxies also affect the results of the detection process. An arc, or part of it, which lies close to a cluster galaxy will sometimes be misclassified as part of that galaxy. The arc can also be broken into two separate segments if a galaxy is positioned on top of it.

We also studied the implications of introducing a lower background into our simulated images. Applying our arc-finding program to the secondary sample of images, mentioned in §3.4, we find that the detection process is affected in several ways: 1) In the lower background images, wider parts of the arcs are detected, thus changing their l/w, sometimes below or above the detection threshold of $l/w \geq 10$.
2) An arc which is detected as two separate arcs in the high-background image can be detected as one continuous arc in the low-background image (see, e.g., Fig. 4). These competing effects seem to largely cancel, as the number of giant arcs and giant luminous arcs in the low-background images was higher by 11 and lower by 3, respectively, than their number in the higher-background images. A systematic study of the influence of these and other observational effects will be presented in Meneghetti et al. (2005, in preparation).

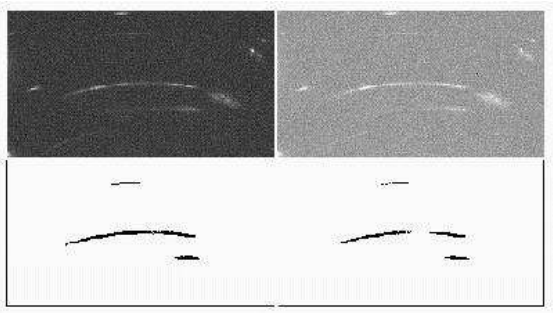

FIG. 4.— Examples of simulated lensed images with low background (top left) and high background (top right). The bottom panels show the arcs detected in each case. A higher background can lead to the apparent break-up of long arcs. On the other hand, a low background can reveal low surface-brightness regions of an arc, leading to an assignment of a lower l/w ratio.

5.2. *Results for the observed sample and comparison with the simulations*

We applied the same arc-finding algorithm described in §4 to the observed sample. Fig. 5 shows the relevant image sections and the arcs identified by the arc finder. A total of 12 arcs with $l/w > 10$ are detected in 7 out of the 10 observed clusters, giving a mean of $1.20^{+0.46}_{-0.34}$ arcs per cluster. Only two of these arcs are giant luminous arcs, i.e., a mean of $0.20^{+0.26}_{-0.13}$ giant luminous arcs per cluster. Before comparing these results to the results of the simulated sample we take into consideration the fact that the area in which the observed arcs were detected, covered by the WFPC2 CCDs, is only a fraction of the total cluster area. Based on the shape of the WFPC2 mosaic, we have calculated the average effective coverage area as a function of the distance from the cluster center. We then assign a detection probability to each detected arc in the simulated sample based on the above function, obtaining $0.71^{+0.06}_{-0.06}$ arcs per cluster and $0.19^{+0.04}_{-0.03}$ giant luminous arcs per cluster. Our simulated results, both for the total number of giant arcs and for the number of giant luminous arcs, are therefore consistent with the observations to within 1.6σ. Examining the observed and the simulated distributions of arc number per cluster, a Kolmogorov-Smirnov test indicates that the hypothesis that both distributions are drawn from the same parent distribution can be only marginally rejected, with a probability of 96.7%. The difference is in the sense that real clusters produce a flatter distribution – fewer clusters are arcless and more clusters have two giant arcs. As seen in Fig. 6, the small number of observed clusters dominates the uncertainty in the comparison. Larger observed samples can therefore allow more stringent tests.

Additional statistical properties are consistent between the observed and simulated samples. Figure 7 compares the distributions of arc lengths, widths, and l/w ratios. All of them show consistency between the lensing efficiency predicted by the simulated ΛCDM clusters and the observed data.

6. CONCLUSIONS

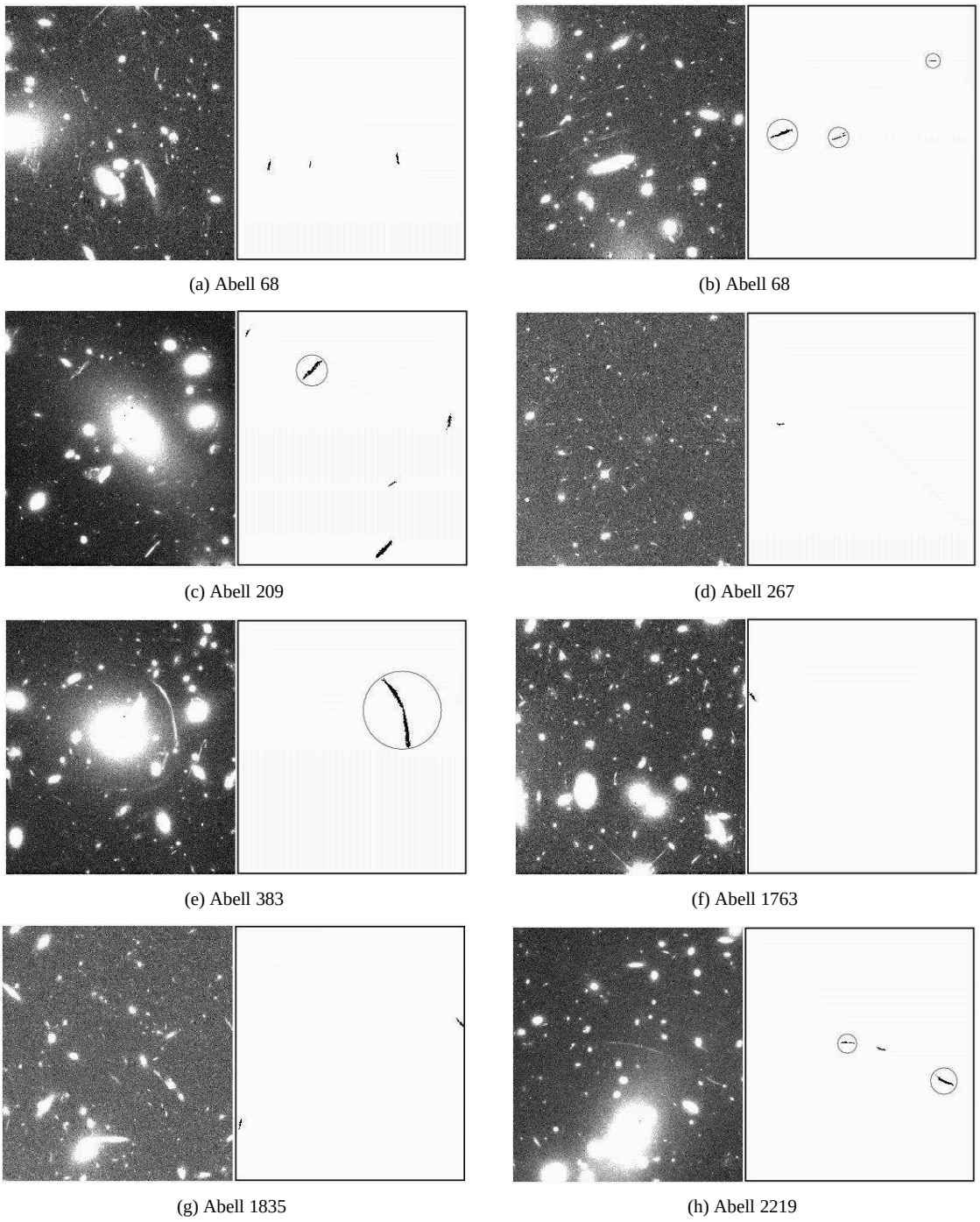

(a) Abell 68

(b) Abell 68

(c) Abell 209

(d) Abell 267

(e) Abell 383

(f) Abell 1763

(g) Abell 1835

(h) Abell 2219

FIG. 5.— $62'' \times 69''$ sections of WFPC2 images of the observed clusters with arcs, showing only the regions in which arcs are detected. The right hand panels show the arcs (with $l/w \geq 7$) detected in each case by our automated arc-finding algorithm. Giant arcs ($l/w \geq 10$) are circled.

We have carried out a comparison of the arc-production efficiency of an observed sample of massive clusters, and of a sample of clusters produced in a ΛCDM N-body simulation. The two samples are roughly matched in mass. In our simulations we have used a realistic source population, in the form of the HDF, including the number density, surface brightness profiles, and redshifts of the galaxies in it. We have attempted to simulate the observational effects that may influence arc statistics. Finally, we have carried out an objective comparison of the two samples, not limited by arc brightness, by applying to both samples an automatic arc-finding algorithm.

Our main result is that the lensing efficiencies of the observed and the simulated clusters are consistent. The observed clusters may be somewhat more efficient lenses than the simulated clusters based on the total number of giant arcs they produce, or on the distribution of the number of arcs per cluster, but the differences are marginally significant (1.6σ and 2.1σ, respectively) and could well be due to small number statistics. The above differences could also be explained if the lensing efficiency correlates with mass, since the observed clusters go to somewhat higher masses than the simulated ones. We note, however, that the most massive cluster in the observed sam-

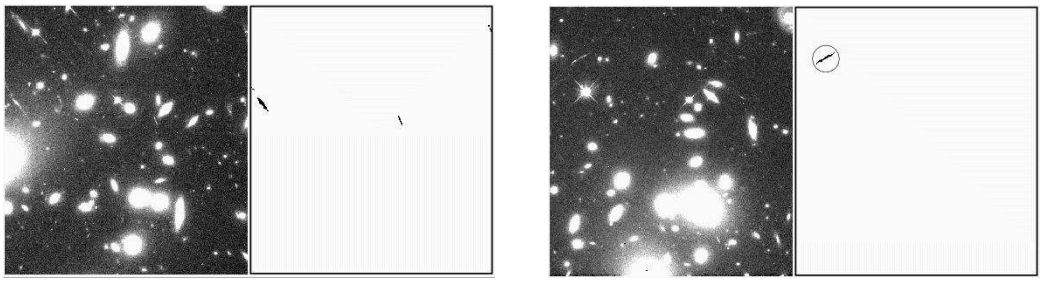

(i) Abell 773 (j) Abell 773

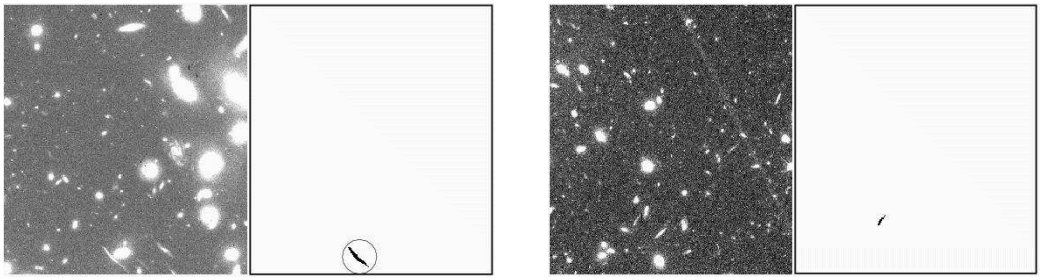

(k) Abell 773 (l) Abell 963

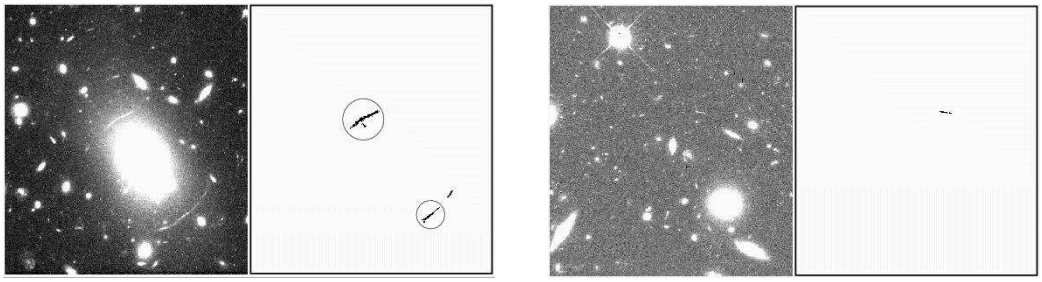

(m) Abell 963 (n) Abell 963

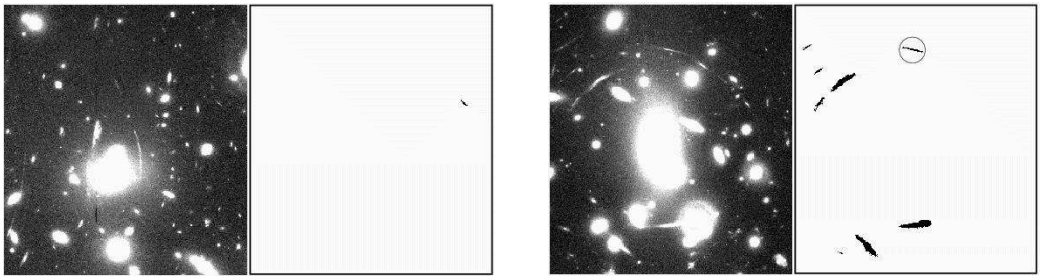

(o) Abell 2218 (p) Abell 2218

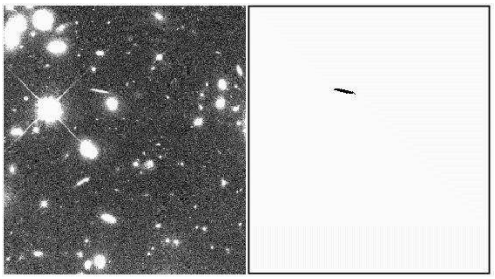

(q) Abell 2218

FIG. 5.— [continued]

ple, Abell 1835, has no detected giant arcs, and in the mass range of our observed and simulated clusters the lensing efficiency may have a weak dependence on cluster mass (e.g., Hennawi et al. 2005).

Given that we have used the same $z_c = 0.2$ N-body cluster sample as B98, it is instructive to compare our results. We find that the number of giant luminous arcs produced by the clusters is higher by a factor of ~ 3 than the number obtained by

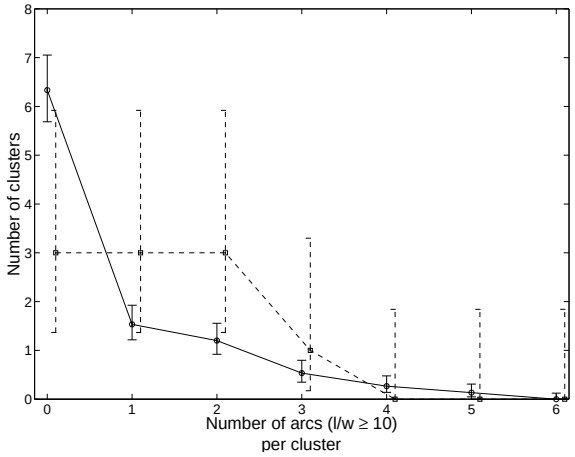

FIG. 6.— Distributions of arcs per cluster with $l/w \geq 10$ for the observed (squares and dashed lines) and simulated (circles and solid lines) samples. The distribution for the simulated clusters has been normalized to the total number of observed clusters. Poisson errors are indicated.

B98. The difference can be explained by the different background source densities used by us and by B98. According to the Fernández-Soto et al. (1999) photometric redshift catalog, the density of background sources with $R \leq 24$ mag and $0.6 \leq z_s \leq 2$ is $6.5 \times 10^4 \mathrm{deg}^{-2}$, higher by a factor of 3.2 than the density assumed by B98. This result, by itself, is a major step towards solving the order-of-magnitude problem reported by B98. Other differences between our work and B98 seem to have little or no influence on the number of giant luminous arcs. In particular, using a realistic redshift distribution for the background sources, as opposed to placing them all at redshift $z_s = 1$, results in only a small change in the number of giant luminous arcs. We should remember that, contrary to other studies that have investigated the effect of source redshift (e.g., Wambsganss et al. 2004, Dalal et al. 2004, Li et al. 2005), our study also includes simultaneously other effects – source size and surface brightness – which can also be redshift dependent, and which can cancel or reinforce the influence of the redshift on cross section. In any event, our simulations, which are more realistic in this respect than previous ones, show that the total number of arcs is weakly affected by placing all sources at $z_s = 1$ (or at $z_s = 1.5$), rather than at their true redshifts.

As opposed to previous studies, our approach has allowed us to compare the observations and the theoretical predictions also for less luminous arcs. As described above, for such arcs, which are several times as numerous as the luminous ones, there is also agreement between the observed and simulated samples, though with a hint for a higher (factor $\lesssim 2$) lensing efficiency of the observed sample.

Our results point the way to several improvements and extensions that could be implemented in future studies, and which could provide stronger tests of cosmology by means of arc statistics. From the observational aspect, the uncertainties in the present work are dominated by the small number of clusters and arcs in the observed sample. Larger samples of clusters, observed to large depth and at higher resolution with the HST Advanced Camera for Surveys, are becoming available, and could be used for this purpose. Furthermore, the effects of cluster selection criteria on arc statistics need to be investigated. For example, it could be that X-ray luminosity selects clusters that are undergoing merging and that such clusters have enhanced lensing cross-sections. This could then explain the factor ~ 2 enhancement in lensing efficiency of observed clusters suggested by our results, if this enhancement is confirmed. Arc statistics measured in cluster samples selected by other means (e.g., by "red sequence" colors; Gladders & Yee 2000) could test this hypothesis.

On the theoretical side, N-body simulations with higher temporal and spatial resolution can give a more reliable picture of cluster substructure and of the importance of merging events for lensing efficiency. A larger number of clusters and of projections of each clusters are needed, in view of the large scatter we have found in the number of arcs produced by different clusters and by different projections of the same clusters. The mass of the cD galaxy, should also be included in the lensing simulations (Meneghetti et al. 2003), as should the cluster gas component (Puchwein et al. 2005).

Although the background source population we have used is more realistic then those used by previous studies, this can still be improved. The HDF covers a small area (which also forced us to tile it in our simulations), and as a results it may be unrepresentative of the typical source density or redshift distribution. Furthermore, several more magnitudes of depth would allow probing the source population of lensed arcs more reliably. The Hubble Ultra Deep Field could serve for this purpose, once its photometric redshifts have been measured and calibrated.

In summary, we have shown that model ΛCDM clusters at $z_c = 0.2$ have lensing efficiencies similar as to those of observed X-ray selected clusters of similar mass and redshift. Improved arc statistics tests can be based on larger, differently selected, observational samples, and on larger and more sophisticated simulations. Our results do not address the separate issue of whether N-body simulations produce the correct number and mass distribution of clusters as a function of redshift. Although this aspect of the problem was also folded into previous analyses, it would best be examined by means of a direct comparison of the models and the observations, independent of lensing properties.

ACKNOWLEDGEMENTS

We thank A. Gal-Yam and the anonymous referee for comments. This work was supported by the German Israeli Foundation for Scientific Research and Development.

APPENDIX

THE ARC-FINDING PROGRAM

In order to allow an objective and quantitative comparison of arc statistics in our simulations and the observed dataset, and to permit arc searches in large real and simulated datasets, we have devised an automatic arc-finding algorithm. As mentioned in §4, our algorithm is implemented in a simple script that makes repeated calls to SExtractor (Bertin & Arnouts 1996). The script is written in the C language and utilizes the CFITSIO software library[5] (Pence, 1999). The program is available at http://wise-obs.tau.ac.il∼assafh, or on request from the authors. The outline of our algorithm is as follows.

[5] http://heasarc.gsfc.nasa.gov/fitsio

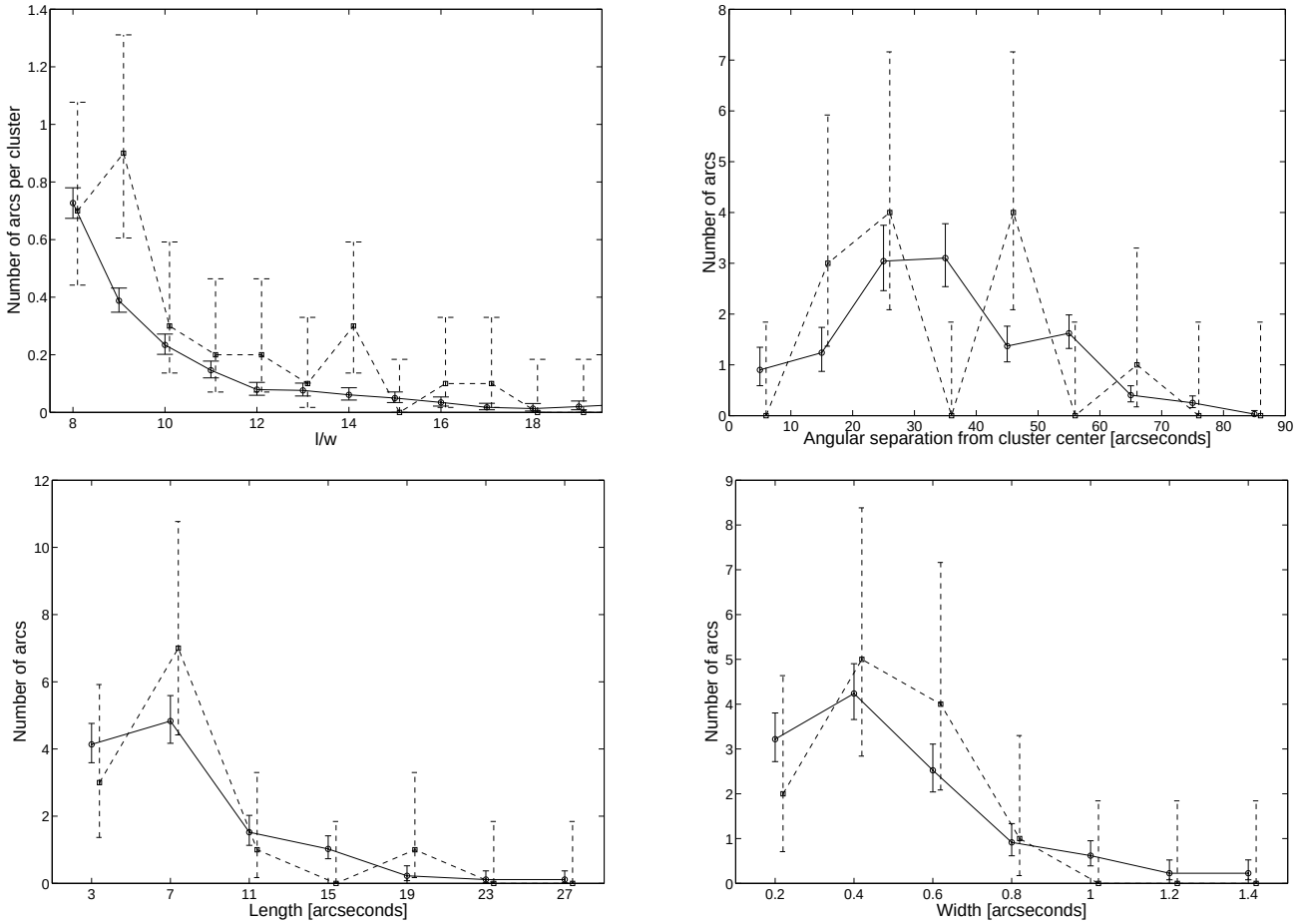

FIG. 7.— Distributions of arc properties. The distributions of lengths, widths, and angular separations from cluster center, are for giant arcs ($l/w \geq 10$). The solid lines represent the simulated sample and the dashed lines the observed sample.

Our algorithm is based on a series of six consecutive detection and elimination SExtractor calls, each using slightly different parameters, as listed in Table A1. After each call, the detected objects which have axis ratios smaller than a set threshold, as listed in Table A1, are eliminated from the detection image. Calls 1, 3, and 5, are applied to the original image, while calls 2, 4, and 6, are applied to the output of calls 1, 3, and 5, in which eliminated objects have been replaced by a constant background. We then combine the three images produced by calls 2, 4, and 6, into a segmentation image in which all non-zero pixels are assigned a constant value. We calculate the l/w ratio, as described in §4, of the objects detected by SExtractor in the combined image. Objects below a user-defined l/w threshold are eliminated from the detection image, thus producing a final image of detected arcs.

TABLE A1
SEXTRACTOR PARAMETERS SETS USED IN THE DETECTION AND ELIMINATION PROCESSES

	Detection and elimination calls					
Parameter name	1	2	3	4	5	6
DETECT_MINAREA	35	35	20	20	20	20
DETECT_THRESH	2σ	2σ	3σ	3σ	4σ	4σ
FILTER	Yes	No	Yes	No	Yes	Yes
DEBLEND_NTHRESH	6	2	6	2	24	24
DEBLEND_MINCONT	0.003	0.01	0.003	0.01	0.001	0.001
Axis ratios eliminated after detection	< 2	< 3.3	< 2	< 3.3	< 2	< 3.3

A different arc finding algorithm has recently been devised by Lenzen et al. (2004). In order to evaluate and compare the performance of our algorithm and of the one of Lenzen et al. (2004), we have applied both of them to the HST images of Abell 2218 and Abell 1689. We set the detection threshold of our algorithm to $l/w \geq 5$ and accordingly set the eccentricity detection parameter to 0.8 in the Lenzen et al. arc detector, while the rest of their arc detection parameters were set according to Fig. 15

from Lenzen et al. (2004). Both algorithms required approximately the same computation time. For example detecting arcs in the 1430×1430 pixel images of Abell 2218, required ~ 1 min of CPU time, running on a computer with an Intel Pentium 4, 2.4 GHz, processor, and with 1 GB of RAM. There is good agreement between the arcs detected by both algorithms. However, the properties of the detected arcs are different. The Lenzen et al. algorithm tends to ignore low surface brightness regions in arcs. Thus, the areas of the arcs detected by the Lenzen et al. arc finder are usually smaller than of those detected by our algorithm. As a result, the arc magnitudes and geometrical properties, such as l/w, will be different. In addition, the arcs detected by the Lenzen et al. arc finder tend to have higher eccentricities, resulting sometimes in false detection of spurious artifacts (see Fig. 15 of Lenzen et al. 2004). These "false positives" are non-arc objects with intrinsically low eccentricity, but for which the algorithm has isolated a high-eccentricity core. In Fig. A1, we illustrate the performance of both algorithms on the two different clusters. For the HST image of Abell 1689, also used for illustration by Lenzen et al., close arcs and arcs which lie next to a galaxy are better resolved by the Lenzen et al. algorithm, while our arc finder sometimes tends to detect two arcs as one, and to associate part of a nearby galaxy with an arc. These differences in performance are similar to the differences already pointed out by Lenzen et al. themselves, when comparing their algorithm to a direct application of SExtractor to cluster images. However when applied to the data for Abell 2218, it appears that the Lenzen et al. program picks out only the highest surface-brightness areas in the arcs, while our arc finder performs better.

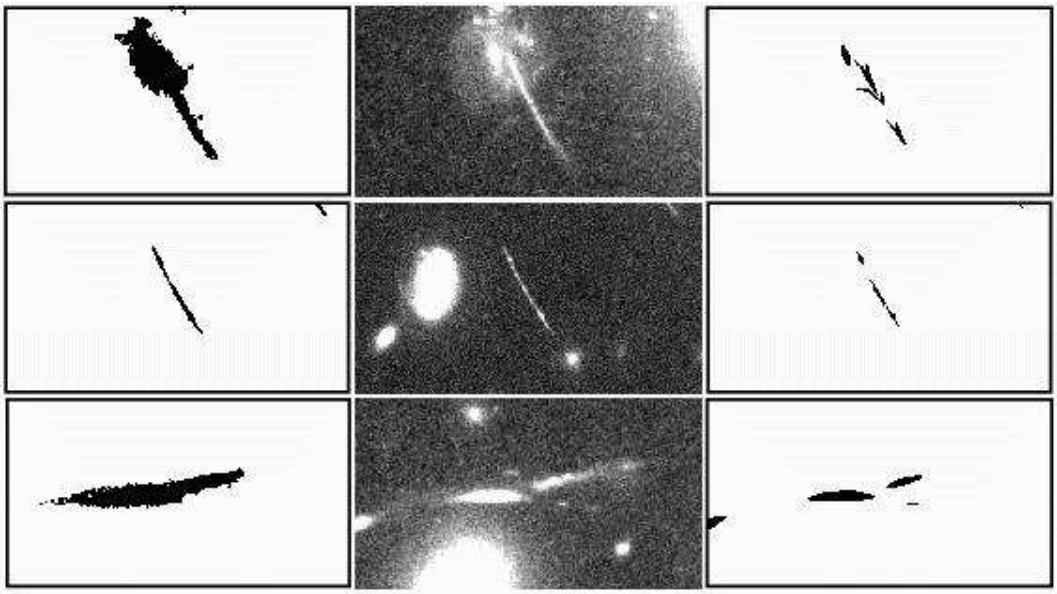

(a) Abell 1689

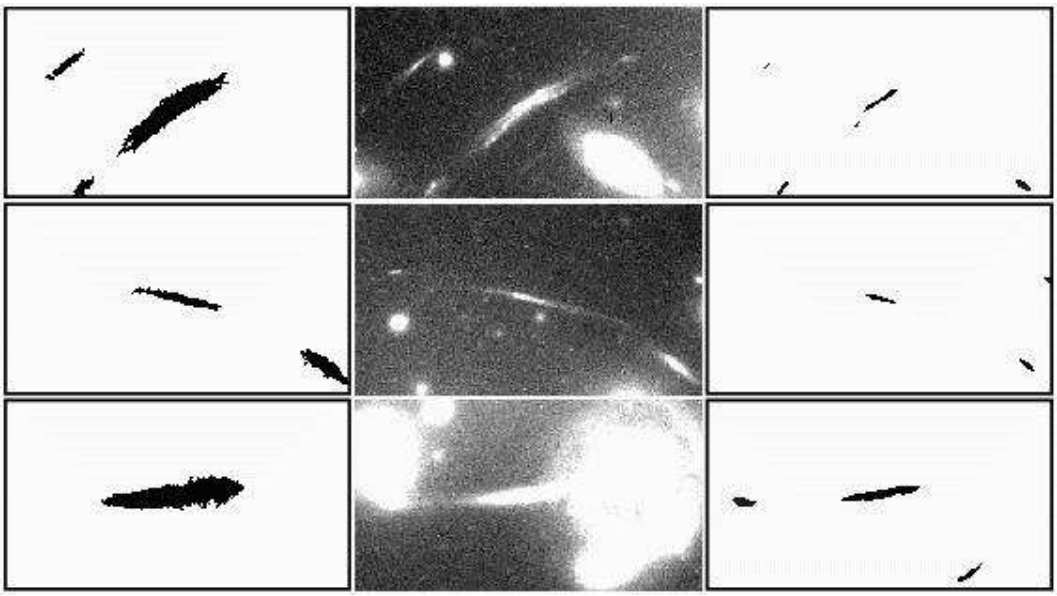

(b) Abell 2218

FIG. A1.— Comparison between arc detection results obtained with our arc finder (left panels) and with the Lenzen et al. (2004) arc detector (right panels). Although generally the same arcs are identified by both algorithms, our arc finder identifies more of the surface area associated with each arc.

To obtain an estimate of the detection efficiencies of both algorithms, we applied them, with a detection threshold of $l/w \geq 10$, to 10 lensing realizations of one of the projections of the simulated cluster cj1409. The "real" arcs were identified by applying our algorithm to each image before the addition of observational effects. We then compared the detection results of both algorithms by comparing them to the "real" arcs by eye. Whenever a "real" arc or a part of it was detected, it was assigned a detection weight of 1, even in cases when it was split into two arcs in the images with the observational effects. Fig. A2 shows the fraction of arcs detected by each algorithm, as a function of magnitude. As seen in Fig. A2, the detection efficiencies of the two algorithms are similar. However, as in the application to the real cluster data, the arcs in the detection images produced by the Lenzen et al. algorithm constitute a small fraction of the total arc areas. In the balance, while the Lenzen et al. arc finder sometimes achieves superior resolution, our algorithm identifies arcs with areas more similar to those picked out by human eyes, and produces fewer false detections.

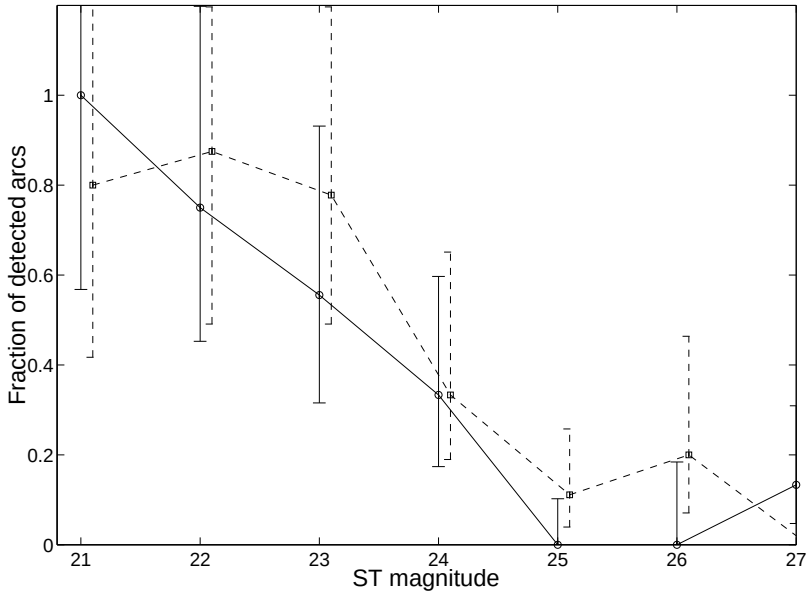

FIG. A2.— Giant arcs $(l/w \geq 10)$ detected in 10 simulated lensed images with observational effects as a fraction of the arcs found in the same images without observational effects, for our arc-finding algorithm (solid line), and the Lenzen et al. (2004) algorithm (dashed line). Poisson errors are indicated.

REFERENCES

Baggett, S., et al. 2002, in HST WFPC2 Data Handbook, v. 4.0, ed. B. Mobasher, Baltimore, STScI

Bartelmann, M., Ehlers, J., & Schneider, P. 1993, A&A, 280, 351

Bartelmann, M., & Weiss, A. 1994, A&A, 287, 1

Bartelmann, M., Steinmetz, M., & Weiss, A. 1995, A&A, 297, 1

Bartelmann, M., Huss, A., Colberg, J. M., Jenkins, A., & Pearce, F. R. 1998, A&A, 330, 1

Bartelmann, M., Meneghetti, M., Perrotta, F., Baccigalupi, C., & Moscardini, L. 2003a, A&A, 409, 449

Bartelmann, M. 2003b, Gravitational Lensing Winter School, Aussois, 2003; astro-ph/0304162

Bernardi, M., et al. 2003, AJ, 125, 1849

Bertin, E., & Arnouts, S. 1996, A&AS, 117, 393

Bond, J. R., & Efstathiou, G. 1984, ApJ, 285, L45

Caon, N., Capaccioli, M., & D'Onofrio, M. 1993, MNRAS, 265, 1013

Dalal, N., Holder, G., & Hennawi, J. F. 2004, ApJ, 609, 50

Dickinson, M. 2000, Building Galaxies; from the Primordial Universe to the Present, 257

Ebeling, H., Voges, W., Bohringer, H., Edge, A. C., Huchra, J. P., & Briel, U. G. 1996, MNRAS, 281, 799

Eke, V. R., Cole, S., & Frenk, C. S. 1996, MNRAS, 282, 263

Fernández-Soto, A., Lanzetta, K. M., & Yahil, A. 1999, ApJ, 513, 34

Flores, R. A., Maller, A. H., & Primack, J. R. 2000, ApJ, 535, 555

Fontana, A., D'Odorico, S., Poli, F., Giallongo, E., Arnouts, S., Cristiani, S., Moorwood, A., & Saracco, P. 2000, AJ, 120, 2206

Gal-Yam, A., Maoz, D., & Sharon, K. 2002, MNRAS, 332, 37

Gladders, M. D., & Yee, H. K. C. 2000, AJ, 120, 2148

Gladders, M. D., Hoekstra, H., Yee, H. K. C., Hall, P. B., & Barrientos, L. F. 2003, ApJ, 593, 48

Goto, T., et al. 2002, PASJ, 54, 515

Hennawi, J. F., Dalal, N., Bode, P., Ostriker, J. P. 2005, preprint astro-ph 0506171.

Kauffmann, G., Colberg, J. M., Diaferio, A., & White, S. D. M. 1999, MNRAS, 303, 188

Kneib, J. P., & Soucail, G. 1996, IAU Symp. 173: Astrophysical Applications of Gravitational Lensing, 173, 113

Le Fevre, O., Hammer, F., Angonin, M. C., Gioia, I. M., & Luppino, G. A. 1994, ApJ, 422, L5

Lenzen, F., Schindler, S., & Scherzer, O. 2004, A&A, 416, 391

Li, Guo-Liang, Mao, S., Jing, Y.P., Bartelmann, M., Kang X., Meneghetti, M. 2005, preprint astro-ph 0503172.

Luppino, G. A., Gioia, I. M., Hammer, F., Le Fèvre, O., & Annis, J. A. 1999, A&AS, 136, 117

Meneghetti, M., Bolzonella, M., Bartelmann, M., Moscardini, L., & Tormen, G. 2000, MNRAS, 314, 338

Meneghetti, M., Bartelmann, M., & Moscardini, L. 2003, MNRAS, 346, 67

Meneghetti, M., Jain, B., Bartelmann, M., Dolag, K., Moscardini, L., Perrotta, F., Baccigalupi, C., & Tormen, G. 2004a, astro-ph/0405070.

Meneghetti, M., Jain, B., Bartelmann, M., & Dolag, K. 2004b, astro-ph/0409030.

Miralda-Escude, J. 1993, ApJ, 403, 509

Pence, W. D. 1999, in ASP Conf. Ser., Vol. 172, Astronomical Data Analysis Software and Systems VIII, eds. D. M. Mehringer, R. L. Plante, & D. A. Roberts (San Francisco: ASP), 487

Puchwein, E., Bartelmann, M., Dolag, K., & Meneghetti, M., 2005, A&A, submitted, astro-ph/0504206.

Reiprich, T. H., & Böhringer, H. 2002, ApJ, 567, 716

Sharon, K. 2003, M.Sc. Thesis, Tel Aviv University.

Schechter, P. 1976, ApJ, 203, 297

Smail, I., Hogg, D. W., Yan, L., & Cohen, J. G. 1995, ApJ, 449, L105

Smith, G. P., Kneib, J.-P., Smail, I. , Mazzotta, P., Ebeling, H., & Czoske, O. 2004, MNRAS, submited(preprint astro-ph/0403588)
Torri, E., Meneghetti, M., Bartelmann, M., Moscardini, L., Rasia, E., & Tormen, G. 2004, MNRAS, 349, 476
Wambsganss, J., Bode, P., & Ostriker, J. P. 2004, ApJ, 606, L93
Williams, R. E., et al. 1996, AJ, 112, 1335
Wu, X., & Hammer, F. 1993, MNRAS, 262, 187
Zaritsky, D., & Gonzalez, A. H. 2003, ApJ, 584, 691